Experimental and Molecular Dynamics Simulation Study of Chemical Short-Range Order in CrCoNi Medium-Entropy Alloy Fabricated Using Laser Powder Bed Fusion

Bolun Han [a,b], Kai Feng [a,b] *, Zhuguo Li [a,b] **, Pan Liu [c,d], Yakai Zhao [e], Junnan Jiang [c,d], Yiwei Yu [a,b], Zhiyuan Wang [a,b], Kaifeng Ji [a,b]

[a] Shanghai Key Laboratory of Materials Laser Processing and Modification, School of Materials Science and Engineering, Shanghai Jiao Tong University, Shanghai 200240, China

[b] Collaborative Innovation Center for Advanced Ship and Deep-Sea Exploration, Shanghai, 200240, China

[c] Shanghai Key Laboratory of Advanced High-temperature Materials and Precision Forming, State Key Laboratory of Metal Matrix Composites, School of Materials Science and Engineering, Shanghai Jiao Tong University, Shanghai, 200240, China

[d] Shanghai Jiao Tong University - JA Solar New Energy Materials Joint Research Center, Shanghai, 200240, China

[e] Institute of Materials Research and Engineering (IMRE), Agency for Science, Technology and Research (A*STAR), Singapore 138634, Republic of Singapore

**Corresponding Authors:*

Prof. Kai Feng: E-mail: fengkai@sjtu.edu.cn

Prof. Zhuguo Li: E-mail: lizg@sjtu.edu.cn

Abstract

CrCoNi medium-entropy alloy (MEA) fabricated by laser powder bed fusion (LPBF) benefits from its distinctive hierarchical microstructure and has great potential as a structural material. However, while the intriguing chemical short-range order (CSRO) widely exists in high/medium entropy alloys, its formation in the LPBF-built samples still lacks enough understanding. In this study, we verified its existence by fine transmission electron microscopy characterizations and utilized hybrid Monte Carlo/Molecular Dynamics simulations to investigate the features and effects of CSRO in LPBF-built CrCoNi MEA (AM model). Results showed that the CSRO fraction and the stacking fault energy of the AM model lie between those of the well-annealed and random solid solution counterparts. Among these models, the AM model exhibited the best strain hardening ability due to its highest capability to generate and store sessile dislocations. The results agreed well with existing data and provide guidance to the future development of LPBF-built CrCoNi MEA.

Keywords: Laser powder bed fusion; Medium-entropy alloy; Chemical short-range order; Monte Carlo/molecular dynamics simulation

Since its first presence in 2004 [1], high entropy alloy (HEA) has been progressively studied for its great potentials in many industries. Among the major families of HEAs, the CrCoNi medium entropy alloy (MEA), a subset of the CrMnFeCoNi "Cantor" alloy [2], has attracted a lot of attention due to its twinning-induced plasticity (TWIP) effect and dynamic "Hall-Petch" effect which contribute to continuous strain hardening [3, 4]. Moreover, the intriguing chemical short-range order (CSRO) in CrCoNi (and other MEA/HEAs) has raised growing attention [5-7] for its distinctive effect to the overall mechanical properties. CSRO was reported to act as nucleation sites for Shockley partial (SP) generation but barrier for SP propagation, and therefore promote nano-twinning [5]. Zhang *et al*. reported that the stacking fault energy (SFE) would increase with increasing amount of CSRO, and therefore introduced new way of tuning the mechanical properties [6]. Recently, Yang *et al*. [7] concluded that the destruction of CSRO during gliding and local material rejuvenation is the sequence of the key deformation mechanisms such as nano-twinning. CSRO may only have positive effect on the mechanical performance of metallic materials, and it still needs further explorations and verifications [8].

Previous studies were mostly focused on materials fabricated by conventional processing methods including casting, rolling, and heat treatments [6-10]. The low cooling rates and ample time of diffusion is beneficial for CSRO formation in these processes. Besides, only a small part of CSROs would be destroyed during mechanical deformation and most of them would survive in many cases [7, 8]. Therefore, most of the CSRO features tend to be preserved in ready-to-use parts produced by these methods during the long thermal mechanical processes involving solidification, cooling, and heat treatments. However, during laser-based additive manufacturing (AM) such as laser powder bed fusion (LPBF), an ultra-high cooling rate of 10^6–10^7 K/s could be

achieved [11] in contrast to the low cooling rates in achieved casting. This could potentially result in distinctive CSRO features of LPBF-built metallic materials such as different CSRO intensity, and subsequently influence the mechanical properties in a new aspect. The additively manufactured CrCoNi MEA and its collateral systems have been actively studied in recent years and superior mechanical properties have been reported [12-14], but the CSRO features in it were seldomly investigated [15]. Keeping these in view, this study focuses specifically on the CSRO in LPBF-built CrCoNi MEA, and its presence, intensity, and effects on the mechanical properties were systematically investigated through coupled experiments and molecular dynamics (MD) simulations.

A Trumpf TruPrint 1000 metal printer was used to build bulk parts by LPBF with the following parameters: laser power - 180 W, scanning speed - 1100 mm/s, hatch spacing - 50 μm, and layer thickness - 30 μm. The parameters used were identical to those used in our previous work [12]. The specimens (in 5×5×5 mm^3 blocks) were cut off from the substrate by electrical discharge machining (EDM), mechanically ground into 100 μm thick plates, and punched into wafer-like pieces with 3 mm diameter. They were finally thinned by twin-jet polishing using an electrolyte (7% $HClO_4/C_2H_5OH$) at −20 °C with a 25 V voltage for transmission electron microscopy (TEM, TalosF200x field-96 emission TEM, 200 kV) characterization.

Since MC/MD simulations were proved useful to introduce CSRO into CrCoNi MEA [5], they were carried out here using LAMMPS [16] packages with the atomic configurations visualized using Ovito [17] software. The embedded atom method (EAM) potential for the MD simulations used in this study was developed by Li *et al*. [18]; the timestep in these simulations is 1 fs. The LPBF simulation model consists of 720,000 atoms with *x*, *y*, and *z* along the <100> crystal directions, given the (100) growth texture found in LPBF-built CrCoNi MEA [12]. The dimensions of the

simulation box are 106.59×106.59×710.6 $Å^3$ (30×30×200 unit cells, lattice parameter a_0=3.553 Å [12]). Periodic boundary conditions were applied in all the directions. Similar to that used by Antillon *et al*. [19], the center part of the model was defined as substrate region while the rest parts as the melt pool regions. The thickness of the substrate region was 71.06 Å (20 unit cells). First, to simulate melting, the temperature of the melt pool regions was raised to 2000 K in 100 ps under a canonical (NVT) ensemble, while the temperature of the substrate region was kept at room temperature (RT, 300 K) under an isothermal-isobaric (NPT) ensemble to avoid conflicted box alternation. Second, to simulate solidification, after the temperature reaches the maximum, the entire simulation model was "quenched" to RT in 1600 ps under an NPT ensemble. After completing the cooling process, a specific cubic region (64.01×63.48×63.78 $Å^3$, 22,041 atoms) inside the solidified molten pool (denoted as "AM" hereafter) was selected and rotated till its [111] // *z* to evaluate the Warren-Cowley parameter (WCP) and SFE.

Parallel to the AM simulation for LPBF specimens, the comparative well-annealed CrCoNi model (achieved by MC/MD and denoted as "MC/MD" hereafter) and the CrCoNi random solid solution model (denoted as "RSS") were created in a similar simulation domain with the same crystalline orientations as the AM model. The RSS and MC/MD models are cubes with their three orthogonal edges parallel to $[01\bar{1}]$, $[2\bar{1}\bar{1}]$, and [111], respectively. The dimensions of the cubes are 50.25×87.03×61.54 $Å^3$ (20×20×10 cells, 24000 atoms) and were determined by the SFE convergence tests (the aforementioned dimensions of the AM model were determined accordingly). While Ni, Co, and Cr atoms are randomly distributed in the RSS model, the positions of different atoms in the MC/MD model were exchanged following a certain probability (dictated by the Metropolis criterion [20]) to reach the configuration with the minimal energy

(MC annealing). Simultaneously an NPT ensemble was employed to achieve relaxation (MD relaxation) for 40 ps. Therefore, the MC/MD simulation functioned like a low temperature annealing treatment for a very long time, mimicking the various heat treatment methods used in the industry. For each run on the MC/MD model, 120 MC swaps were attempted every 20 timesteps (240,000 swap attempts in total) for both Ni/Cr swap and Ni/Co swap with no chemical potential specified.

To simulate deformation, full-size MC/MD and RSS models (with identical dimensions to the full-size AM model, denoted as "MC/MD_{deform}" and "RSS_{deform}" hereafter) were created using the corresponding approaches described above. The AM_{deform} model was created using the solidified LPBF model with the LPBF-produced dislocations at both ends removed (see **Fig.3d**) to avoid early deformation-induced nucleation of dislocations and twinning. Note that some vacancies were kept, which have little effect on the mechanical responses. The AM_{deform} model consists of 665919 atoms with a simulation cell of 106.82×106.77×658.5 $Å^3$ (30×30×185 unit cells). It was annealed to relief residual stress under an NPT ensemble of 300 K for 40 ps. For subsequent uniaxial deformation along *x*, a strain rate of 0.001 ps^{-1} was used. The definition and calculation of Warren-Cowley parameter (WCP) and SFE is available in supplementary information.

Results of the TEM characterization conducted on the LPBF-built CrCoNi MEA are shown in **Fig.1**. **Fig.1e** shows a typical cellular microstructure, that is widely reported in alloys with the FCC crystal structures [21]. An area free of dislocations and other defects was chosen (**Fig.1a**) to perform selected area electron diffraction (SAED) pattern obtained along [112] direction. The SAED results are shown in **Fig.1b$_1$** and its enhanced version **Fig.1b$_2$**, with brightness and contrast refined. The demonstrated extra superlattice spots at $1/2\{1\bar{3}1\}$ sites are a distinctive feature of extra periodicity beside

the basic FCC lattice. It has been reported that some other defects, such as SF tetrahedra and Frank dislocation loops, can have similar effect as CSRO which introduces extra spots in SAED pattern [22, 23]. Since a defect-free area was selected for SAED here, these extra spots should be identified as the proof of the existence of CSRO [24, 25]. It is noted that the intensity of extra spots is weaker than that from the FCC matrix, indicating a relatively weak CSRO intensity. A Fourier-filtered version (by removing non-periodic contrasts, e.g. the thickness contrast) of the high-resolution TEM (HRTEM) image obtained from a certain part of the microstructure (displayed in **Fig.1e**) is shown in **Fig.1c**. The inlet of **Fig.1c** shows the Fast Fourier Transformation (FFT) of **Fig.1c**, representing its diffraction result. Subsequently, the inversed FFT (IFFT) result of the extra 1/2{1$\bar{3}$1} spots (the red-colored pattern) was superimposed with **Fig.1c** (the blue-colored parts) and shown in **Fig.1d**, demonstrating the existence of CSRO in LPBF-built CrCoNi MEA. Consequently, the lattice distance of {1$\bar{3}$1} planes have the corresponding relationship: $\lambda_{CSRO} = 2\lambda_{FCC}$.

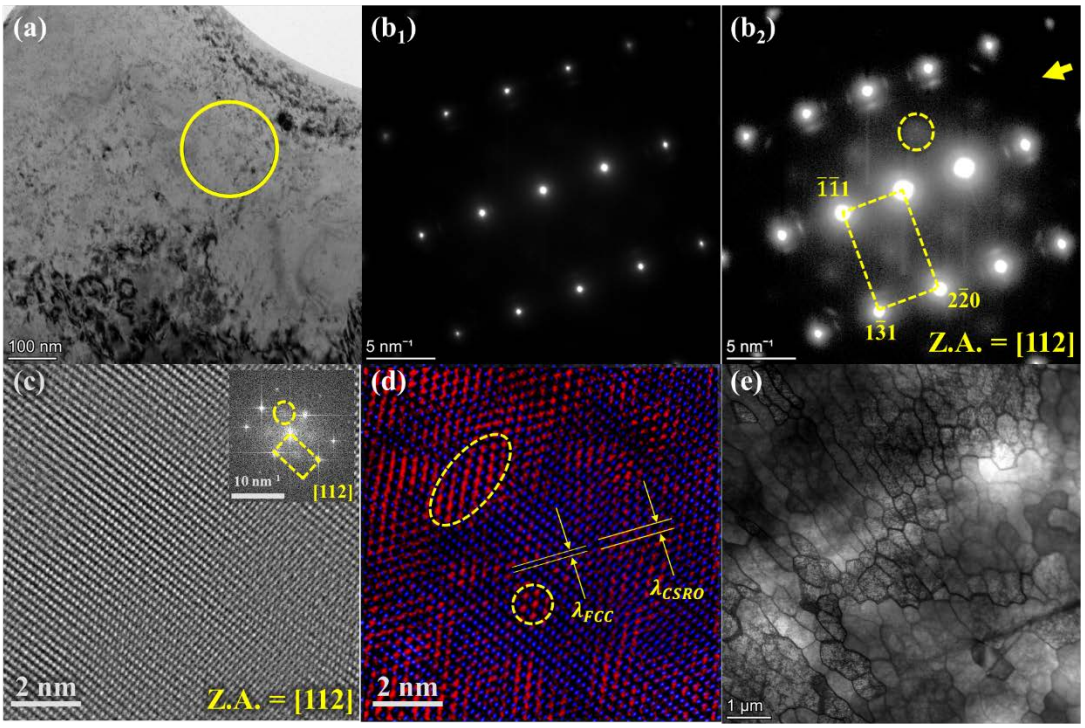

Fig.1 Experimental proof of CSRO existence. (a) TEM image of the selected defect-free zone for SAED. (b_1-b_2) [112] diffraction patterns showed extra 1/2{$1\,\bar{3}\,1$} superlattice spots. (b_2) is the enhanced version of (b_1) with brightness and contrast refined; (c) Fourier-filtered HRTEM image and its SAED; (d) picture showing the presence of CSRO by superimposing the IFFT of extra spots and the filtered HRTEM matrix. The yellow dashed circle highlights the clustering of CSRO; (e) as-built cellular microstructure.

After confirming the existence of CSRO in the LPBF-built CrCoNi MEA, a series of MD simulations were performed to evaluate its influence on the macroscopic mechanical properties. Three models were used for the comparative simulations. First, to simulate the rapid melting and solidification in the LPBF process reimage the CSRO in the system, a simulated LPBF process was performed per the previous descriptions, with the results shown in **Fig.2**. The substrate and melt pool regions and their evolution during simulated LPBF were shown in **Fig.2a$_{1\text{-}8}$**. Note that the green atoms are recognized by the common neighbor analysis modifier (CNA) in Ovito as FCC structured, while the white atoms are marked as “Other” which is not within any crystalline structure (molten liquid) in this simulation. In the melting stages shown **Fig.2a$_{1\text{-}4}$,** due to the limitation of NVT “heating” used in the simulation, it is noted that not all atoms in the melt pool region liquefied simultaneously. However, during the cooling stages shown in **Fig.2a$_{5\text{-}8}$**, the simulated directional solidification process corresponds well to the thermal gradient-induced directional solidification in real LPBF [26]. The structure fraction-time curves and the solid-liquid (S-L) interface position curves were shown in **Fig.2b**. The position was determined when the “solidified” region contained 99.9 % of the FCC atoms. The solidification velocity was then measured to be 77.2 m/s based on stage **a$_6$-a$_7$**. **Fig.2c** represents the evolution during solidification

of the concentration distribution of Cr, Co, and Ni in solid (S) and liquid (L). A uniform elemental distribution over the S-L interface was seen during the entire cooling stage ($k_v = x_s/x_l = 1$ in which k_v is the non-equilibrium partition coefficient), indicating complete solute trapping and therefore non-equilibrium solidification [19]. In summary, these results substantiate the fidelity of our MD simulation for reconstructing the LPBF process.

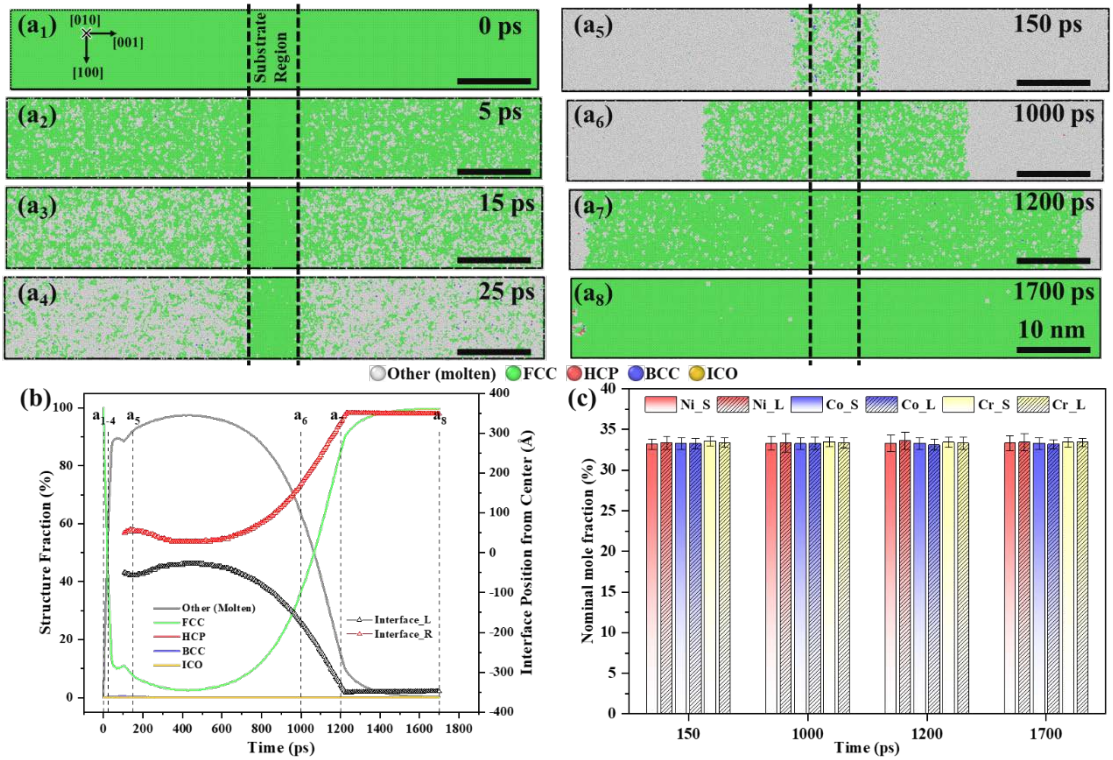

Fig.2 MD simulation results of LPBF process. ($a_{1\text{-}4}$) Snapshots of melting stages and ($a_{5\text{-}8}$) cooling stages. (b) The structure fraction-time curves and the S-L interface position curves. The interface position was determined when the "solidified" region contained 99.9 % of the FCC atoms. (c) The concentrations of Cr, Co, and Ni in solid (S) and liquid (L) regions during the cooling stages. No concentration difference was seen between liquid and solid phases, which indicated complete solute trapping.

After simulating the LPBF process, the cubic AM model was cut out from the two ends as shown in **Fig.3a**. It was carefully refined to keep its periodicity and to avoid vacancies and dislocations that naturally form during the process. Therefore, the dimensions of the AM model ranged from 60.25×52.55×63.78 $Å^3$ (14975 atoms) to 60.75×57.08×63.78 $Å^3$ (15600 atoms). In the atomic configurations of the three models shown in **Fig.3b** (Z.A. = [$\bar{2}$11]), significant clustering of Ni atoms and Co-Cr pairs are clearly visible in AM and MC/MD models. Due to the limitations of frequently used software, we did not manage to perform simulated SAED on the three models to couple with the experimental results. However, it was later confirmed through the WCP calculation that the CSRO intensity of the AM model was weaker than that of the MC/MD model, but much stronger than that of the RSS model. Such phenomena are directly related to the different cooling rates according to solidification theories. The higher the cooling rate, the weaker the CSRO would be as there would be less time for the atoms to diffuse.

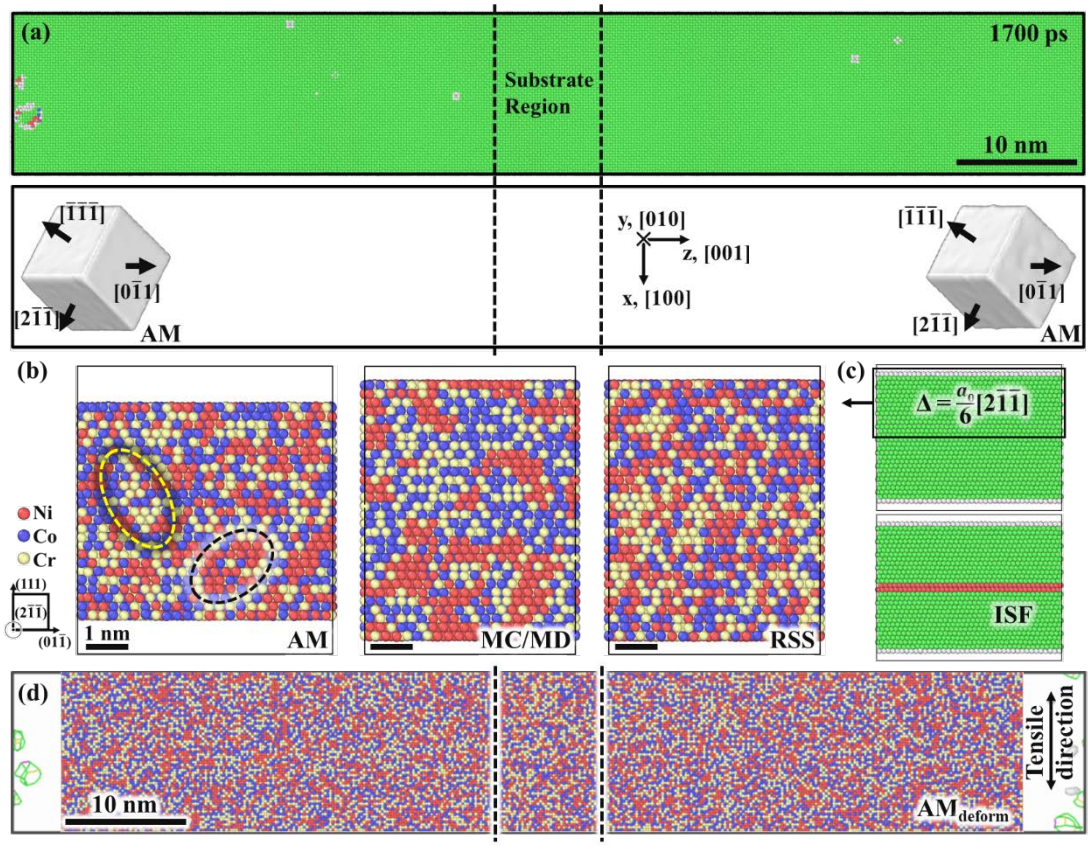

171

172 **Fig.3** Comparison of three models. (a) Schematic of how the AM model was created
173 based on the solidified LPBF model. (b) Comparison of atomic configurations. (c)
174 Schematic of intrinsic SFE calculation. (d) Schematic of how the AM_{deform} model was
175 created. Two ends containing as-built dislocations and vacancies were removed.

176 Finally, the deformation simulation results, including the stress-strain curves, HCP
177 phase fraction evolution, and dislocation density evolution, of the three models were
178 shown in **Fig.4a-b.** Due to the absence of defects and other inherent disadvantages of
179 MD [5], mechanical properties obtained by simulated deformation in MD are not
180 comparable to the experimental values. Nevertheless, a qualitative comparison among
181 samples shall still be valid and can offer valuable insights. Other results including WCP,
182 SFE, yield strength (YS), critical strain of dislocation and HCP nucleation ($\varepsilon_{dislocation}$
183 and ε_{HCP}), maximum sessile dislocation density (max. $\rho_{sessile}$) and flow stress of the three
184 models are also shown in **Fig.4c-d**. The exact values of the parameters shown in **Fig.4c-**

d are available in supplementary information. Here $\varepsilon_{dislocation}$ and ε_{HCP} are used to evaluate the material's ability to generate dislocations and SF/twinning (which is recognized as HCP phase in Ovito). In **Fig.4a**, the MC/MD_{deform} model has higher YS than the AM_{deform} model, which has slightly higher YS than the RSS_{deform} model. However, the AM_{deform} and RSS_{deform} model exhibited better capability to generate and store deformation-induced dislocations SF/twinning, as shown in **Fig.4b** and **Fig.4d**. This is due to the "softening" (decrease in strength) from earlier nucleation of the two deformation mechanisms, which is beneficial to the strength-ductility combination for structural materials [27].

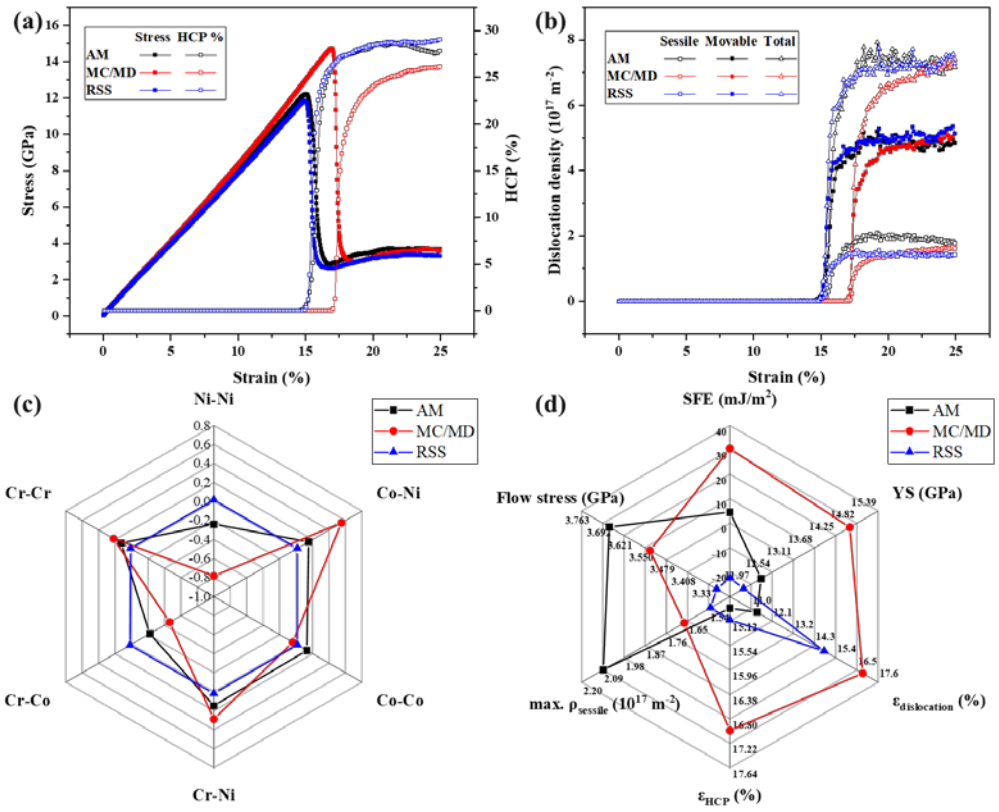

Fig.4 Results of (a, b) deformation simulations, (c) WCP calculations and (d) other valuable results of the AM, MC/MD, and RSS models. Sessile dislocations include 1/6<110>stair-rod and 1/3<001>Hirth dislocations. Movable dislocations include

1/2<110>perfect, 1/6<112>Shockley, and 1/3<111>Frank dislocations. All dislocation types were identified using the dislocation analysis modifier (DXA) in Ovito. The flow stress was defined as the average stress on the strain section from 20 % to 25 %. $\varepsilon_{\text{dislocation}}$ and ε_{HCP} were determined when the first dislocation showed up and when the HCP phase fraction first exceeded 0.2 %, respectively.

It was reported that the intensity of the CSRO is proportional to the absolute value of WCP [28] while the probability of twinning is negatively correlated to SFE [29]. For the RSS model, the WCP values were near zero (as expected), while the SFE values are in accord with reported calculated data [30, 31]. For the MC/MD model, the thermodynamically favored ordering is directly reflected by the high SFE and the absolute values of WCP, which are close to the experimental values reported for a cast, homogenized, swaged, and recrystallized CrCoNi MEA [3]. In comparison, SFE and the absolute value of WCP of the AM model are between the other two models. These results imply a proportional relationship between the WCP and SFE values. Such tendency could be reasonably explained by solidification theory: the equivalent cooling rates during the solidification of the three models decrease from the infinitely fast of the RSS model, close to real additive manufacturing of the AM model to the infinite slow of the MC/MD model. This tendency also explains the mechanical performances of the three models: higher WCP indicated more intense CSRO, which means stronger resistance to dislocation and SF/twinning nucleation [5]. It is noted the AM model has the highest flow stress, owing to its best capability to generate and store sessile dislocations, which contributed to continuous strain hardening during plastic deformation [32, 33]. Since the RSS and MC/MD model show similar behavior, the

reason of such mechanical response may be merely slightly relevant to CSRO and will be explored in the future.

In summary, we confirmed the existence of CSRO in an LPBF-built CrCoNi MEA using detailed TEM characterization, and successfully reimaged the system using MD simulations. With the formation of CSRO captured, its intensity and correlations with the macroscopic mechanical properties were evaluated and compared with other two commonly used systems. Results showed that in these three systems, (1) the absolute value of WCP is proportional to SFE and YS; (2) the AM model is the best to generate dislocations and SF/twinning; (3) the AM model has the highest strain hardening capability due to highest sessile dislocation density. The results showed good correspondence with existing experimental and calculated data and explained the remarkable mechanical properties of LPBF-built CrCoNi MEA from a new aspect.

Acknowledgments

This work was financially supported by National Key R&D Program of China (No. 2022YFB4602102), National Natural Science Foundation of China (Grant No. 51971144), Natural Science Foundation of Shanghai (Grant No.19ZR1425200). Special thanks go to A. Prof. Wentao Yan from National University of Singapore, A. Prof. Wenhu Lin from ShanghaiTech University, Dr. Mingxu Wang from Shandong University, and Dr. Daijun Hu from National University of Singapore.

References

[1] J.-W. Yeh, Recent progress in high-entropy alloys, Annales de Chimie Science des Matériaux 31(6) (2006) 633-648.

[2] B. Cantor, I.T.H. Chang, P. Knight, A.J.B. Vincent, Microstructural development in equiatomic multicomponent alloys, Mater. Sci. Eng., A 375-377 (2004) 213-218.

[3] G. Laplanche, A. Kostka, C. Reinhart, J. Hunfeld, G. Eggeler, E.P. George, Reasons for the superior mechanical properties of medium-entropy CrCoNi compared to high-entropy CrMnFeCoNi, Acta Mater. 128 (2017) 292-303.

[4] S. Huang, H. Huang, W. Li, D. Kim, S. Lu, X. Li, E. Holmstrom, S.K. Kwon, L. Vitos, Twinning in metastable high-entropy alloys, Nat. Commun. 9(1) (2018) 2381.

[5] W.-R. Jian, Z. Xie, S. Xu, Y. Su, X. Yao, I.J. Beyerlein, Effects of lattice distortion and chemical short-range order on the mechanisms of deformation in medium entropy alloy CoCrNi, Acta Mater. 199 (2020) 352-369.

[6] R. Zhang, S. Zhao, J. Ding, Y. Chong, T. Jia, C. Ophus, M. Asta, R.O. Ritchie, A.M. Minor, Short-range order and its impact on the CrCoNi medium-entropy alloy, Nature 581(7808) (2020) 283-287.

[7] Y. Yang, S. Yin, Q. Yu, Y. Zhu, J. Ding, R. Zhang, C. Ophus, M. Asta, R.O. Ritchie, A.M. Minor, Rejuvenation as the origin of planar defects in the CrCoNi medium entropy alloy, Nat. Commun. 15(1) (2024) 1402.

[8] X. Wu, Chemical short-range orders in high-/medium-entropy alloys, Journal of Materials Science & Technology 147 (2023) 189-196.

[9] Y. Zhao, J.-M. Park, J.-i. Jang, U. Ramamurty, Bimodality of incipient plastic strength in face-centered cubic high-entropy alloys, Acta Mater. 202 (2021) 124-134.

[10] A.M.Z. Tan, Z. Li, Y. Zhao, U. Ramamurty, H. Gao, Modeling the improved hydrogen embrittlement tolerance of twin boundaries in face-centered cubic complex concentrated alloys, Journal of the Mechanics and Physics of Solids 188 (2024).

[11] S. Kavousi, V. Ankudinov, P.K. Galenko, M. Asle Zaeem, Atomistic-informed kinetic phase-field modeling of non-equilibrium crystal growth during rapid solidification, Acta Mater. 253 (2023).

[12] B. Han, C. Zhang, K. Feng, Z. Li, X. Zhang, Y. Shen, X. Wang, H. Kokawa, R. Li, Z. Wang, P.K. Chu, Additively manufactured high strength and ductility CrCoNi medium entropy alloy with hierarchical microstructure, Mater. Sci. Eng., A 820 (2021).

[13] J. Wang, J. Zou, H. Yang, L. Zhang, Z. Liu, X. Dong, S. Ji, Exceptional strength-ductility synergy of additively manufactured CoCrNi medium-entropy alloy achieved by lattice defects in heterogeneous microstructures, Journal of Materials Science & Technology 127 (2022) 61-70.

[14] N. Yao, T. Lu, K. Feng, B. Sun, R.-Z. Wang, J. Wang, Y. Xie, P. Zhao, B. Han, X.-C. Zhang, S.-T. Tu, Ultrastrong and ductile additively manufactured precipitation-hardening medium-entropy alloy at ambient and cryogenic temperatures, Acta Mater. 236 (2022).

[15] E. Ma, C. Liu, Chemical inhomogeneities in high-entropy alloys help mitigate the strength-ductility trade-off, Prog. Mater Sci. 143 (2024).

[16] A.P. Thompson, H.M. Aktulga, R. Berger, D.S. Bolintineanu, W.M. Brown, P.S. Crozier, P.J. in 't Veld, A. Kohlmeyer, S.G. Moore, T.D. Nguyen, R. Shan, M.J. Stevens, J. Tranchida, C. Trott, S.J. Plimpton, LAMMPS - a flexible simulation tool for particle-based materials modeling at the atomic, meso, and continuum scales, Computer Physics Communications 271 (2022) 108171.

[17] A. Stukowski, Visualization and analysis of atomistic simulation data with OVITO–the Open Visualization Tool, Modelling and Simulation in Materials Science and Engineering 18(1) (2010) 015012.

[18] Q.J. Li, H. Sheng, E. Ma, Strengthening in multi-principal element alloys with local-chemical-order roughened dislocation pathways, Nat. Commun. 10(1) (2019) 3563.

[19] E.A. Antillon, C.A. Hareland, P.W. Voorhees, Solute trapping and solute drag during non-equilibrium solidification of Fe–Cr alloys, Acta Mater. 248 (2023).

[20] N. Metropolis, A.W. Rosenbluth, M.N. Rosenbluth, A.H. Teller, E. Teller, Equation of state calculations by fast computing machines, The Journal of Chemical Physics 21(6) (1953) 1087-1092.

[21] L. Liu, Q. Ding, Y. Zhong, J. Zou, J. Wu, Y.-L. Chiu, J. Li, Z. Zhang, Q. Yu, Z. Shen, Dislocation network in additive manufactured steel breaks strength–ductility trade-off, Mater. Today 21(4) (2018) 354-361.

[22] F. Walsh, M. Zhang, R.O. Ritchie, A.M. Minor, M. Asta, Extra electron reflections in concentrated alloys do not necessitate short-range order, Nat. Mater. 22(8) (2023) 926-929.

[23] N. Liu, X. Tian, Q. Liu, B. Gan, J. Ding, E. Ma, Z. Wang, Aging elevates chemical short-range order and twinning stress in a CrCoNi medium-entropy alloy, Science China Materials 66(11) (2023) 4220-4225.

[24] J. Wang, P. Jiang, F. Yuan, X. Wu, Chemical medium-range order in a medium-entropy alloy, Nat. Commun. 13(1) (2022) 1021.

[25] L. Zhou, Q. Wang, J. Wang, X. Chen, P. Jiang, H. Zhou, F. Yuan, X. Wu, Z. Cheng, E. Ma, Atomic-scale evidence of chemical short-range order in CrCoNi medium-entropy alloy, Acta Mater. 224 (2022).

317 [26] H. Bikas, P. Stavropoulos, G. Chryssolouris, Additive manufacturing methods and
318 modelling approaches: a critical review, Int. J. Adv. Manuf. Technol. 83(1-4) (2015)
319 389-405.
320 [27] G. Laplanche, A. Kostka, O.M. Horst, G. Eggeler, E.P. George, Microstructure
321 evolution and critical stress for twinning in the CrMnFeCoNi high-entropy alloy, Acta
322 Mater. 118 (2016) 152-163.
323 [28] S. Chen, Z.H. Aitken, S. Pattamatta, Z. Wu, Z.G. Yu, D.J. Srolovitz, P.K. Liaw,
324 Y.W. Zhang, Simultaneously enhancing the ultimate strength and ductility of high-
325 entropy alloys via short-range ordering, Nat. Commun. 12(1) (2021) 4953.
326 [29] H. Huang, X. Li, Z. Dong, W. Li, S. Huang, D. Meng, X. Lai, T. Liu, S. Zhu, L.
327 Vitos, Critical stress for twinning nucleation in CrCoNi-based medium and high
328 entropy alloys, Acta Mater. 149 (2018) 388-396.
329 [30] Y.H. Zhang, Y. Zhuang, A. Hu, J.J. Kai, C.T. Liu, The origin of negative stacking
330 fault energies and nano-twin formation in face-centered cubic high entropy alloys,
331 Scripta Mater. 130 (2017) 96-99.
332 [31] C. Niu, C.R. LaRosa, J. Miao, M.J. Mills, M. Ghazisaeidi, Magnetically-driven
333 phase transformation strengthening in high entropy alloys, Nat. Commun. 9(1) (2018)
334 1363.
335 [32] A. Jarlöv, W. Ji, R. Babicheva, Y. Tian, Z. Hu, H.L. Seet, L. Tan, F. Liu, Y. Liu,
336 M.L.S. Nai, U. Ramamurty, K. Zhou, Tailoring short-range order and dislocation
337 evolution in Cr–Co–Ni medium-entropy alloys: A molecular dynamics study, Mater.
338 Des. 240 (2024).
339 [33] K. Gan, D. Yan, Y. Zhang, Z. Li, Origins of strengthening and toughening effects
340 in twinned nanocrystalline alloys of low stacking fault energy with heterogeneous grain
341 structure, Journal of the Mechanics and Physics of Solids 176 (2023).

342